ORIGINAL PAPER

Synthesis of magnetic ZnFe$_2$O$_4$- reduced graphene oxide nanocomposite photocatalyst for the visible light degradation of cationic textile dyes

M. Ayisha Sidiqua[1] · V. S. Priya[1] · Nishath Begum[2] · Noor Aman[2]

Abstract

ZnFe$_2$O$_4$-reduced graphene oxide (rGO) nanocomposite materials are synthesized by hydrothermal cum pyrolysis method using banana leaves as the carbon source for the degradation of malachite green (MG) and basic yellow dyes (BY). ZnFe$_2$O$_4$-rGO (ZB) ratios are varied as 1:6, 1:3, 1:1 and 3:1. XRD shows the presence of ZnFe$_2$O$_4$, rGO and CaSiO$_3$. FE-SEM displays the hierarchical nano-flower type exfoliated rGO layers formed due to the intercalation of ZnFe$_2$O$_4$ nanoparticles in between the graphite layers with a size 15–35 nm. FT-IR confirms the presence of M–O, OH and C–O–C functionalities in the ZB samples. Integration of ZnFe$_2$O$_4$ and rGO appreciably improves the surface area and pore volume to 342 m^2/g and 0.238 cc/g, respectively, for ZnFe$_2$O$_4$-rGO 1:3 (ZB3). All the nanocomposite materials exhibit superparamagnetism with an increase in saturation magnetization on increasing the carbon ratio till ZB3. UV–visible (DRS) indicates that adding carbon into ZnFe$_2$O$_4$ helps to reduce the bandgap from 1.9 to 1.14 eV. Raman spectra validate the presence of the bilayer rGO in the synthesized samples. ZB3 exhibits complete degradation of MG and BY within 60 min of visible light irradiation following pseudo-first-order kinetics. The optimum conditions for MG and BY are obtained at pH 7 and 10, respectively. Higher activity of ZB3 is attributed to its small crystallite size, high surface area, extended visible-NIR light absorption and formation of ZnFe$_2$O$_4$-rGO heterojunction. This study will help in the use of waste biomass for the synthesis of rGO-based photocatalytic material towards waste water treatment.

Keywords ZnFe$_2$O$_4$ · Reduced graphene oxide · Magnetic photocatalyst · Malachite green · Basic yellow

Introduction

Ever increasing demand of potable water for domestic and industrial need has resulted into unprecedented exploitation of surface and underground water bodies. Developing countries, namely India, China, Bangladesh have accelerated their economic growth on the back of textiles, leather, paper printing, foodstuffs industries. In India textile industries contribute a major portion to economic growth [1]. Aqueous solution of acid dyes, basic dyes, mordant dyes, sulphur dyes, azo dyes are the most commonly used textile dye liquor. Cationic dyes such as malachite green and basic yellow 28 are used to impart green and yellow shades to the fabrics, respectively. However, they are reported to cause acute toxicity to aquatic and terrestrial living beings. Because of that, dyes must be removed from the textile effluent before discharging the treated water in the water bodies. Biological, chemical and physical treatments of dye effluent are the conventional treatment methods reported [2].

Biological treatment involves microbial, algal, fungal and enzymatic degradation which take longer time because of slow cell culture formation [3]. Physical methods involve filtration and adsorption, among which filtration is not suitable for dye removal whereas, adsorption is considered more appropriate treatment process. However, toxicity of dyes remains unchanged as it is only physically separated from the effluent water. Comparatively chemical methods such

✉ V. S. Priya
priya@crescent.education

✉ Noor Aman
nooraman_am@crescent.education

[1] Department of Civil Engineering, B.S. Abdur Rahman Crescent Institute of Science and Technology, Vandalur, Chennai 600048, India

[2] Department of Chemistry, B.S. Abdur Rahman Crescent Institute of Science and Technology, Vandalur, Chennai 600048, India

as advanced oxidation process is reported to degrade the dyes into innocuous products, thereby reducing their toxicity [4]. Sunlight-promoted oxidative degradation of dyes by the semiconductors has emerged as an excellent effluent water treatment technique. TiO_2, WO_3, ZnO, Fe_2O_3, g-CN are the most common semiconductor photocatalysts reported for the dye degradation [5, 6]. However, they suffer from limited surface area, fast electron–hole pairs recombination and filtration-based recovery. In this aspect, transition metal ferrites-based magnetic photocatalysts have recently been studied individually or in composite form for the wastewater treatment [7, 8].

Zinc ferrite ($ZnFe_2O_4$) having spinel structure with a bandgap of 1.6–1.9 eV is used for the degradation of several dyes such as rhodamine B, methyl orange, methylene blue and malachite green dyes [9]. Though capable of easy separation from the reaction mixture because of inherent magnetic behaviour, it is still a challenge to improve its surface area to create more reaction sites. In order to overcome the above problem Yang et al., dispersed zinc ferrite on the activated carbon for the desulphurization of H_2S gas [10]. Elsewhere, zinc ferrite-activated carbon hybrid was used for the removal of nitrite and ammonia in aqueous condition [11]. Graphene Oxide (GO) nanocomposite is previously synthesized by modified Hummers method following the hydrothermal, one-step solvothermal, precipitation-hydrothermal and thermo-chemical routes [12]. $ZnFe_2O_4$- reduced graphene oxide (rGO) nanocomposite is used for the applications such as electrochemical ultrasensitive detection, supercapacitor-based charge storage devices, colorimetric detection and also for dye removal [13–16]. Reported synthesis of rGO from the agricultural waste such as banana peel encouraged the current study on the synthesis of magnetic $ZnFe_2O_4$- rGO nanocomposite photocatalyst from the waste banana leaves [13].

In this paper, the synthesis of $ZnFe_2O_4$ rGO nanocomposite photocatalyst from banana leaves is reported towards the degradation of cationic textile dyes. The characterization of synthesized nanocomposites is performed using XRD, FE-SEM, FT-IR, BET, VSM, UV–visible (DRS) and Raman spectra to evaluate the materials nature, composition, size, functional group, surface area, magnetic property, bandgap and chemical bonding.

Methods

Materials used

Zinc nitrate hexahydrate, sodium hydroxide pellets, N-Cetyl-N,N,N Trimethyl ammonium bromide (CTAB) and iron (III) nitrate nonahydrate purified was obtained from Merck chemicals with AR grade. Malachite green and basic yellow was purchased from Loba Chemie with AR grade. They are denoted as MG and BY, respectively. Banana leaves were collected from the nearby agricultural field. Deionized water was used for the synthesis and reaction purpose.

Synthesis of ZnFe$_2$O$_4$

The process involved in synthesis of zinc ferrite is coprecipitation and hydrothermal process. 0.2 M zinc nitrate and 0.4 M ferric nitrate were independently dissolved in 35 mL water. 1 g of CTAB was dissolved in former solution. Both the solutions were mixed together under stirring for 30 min. Subsequently pH was adjusted to 10 using concentrated NaOH. The resultant suspension was sonicated for 30 min. The homogenized suspension was transferred to teflon coated autoclave for hydrothermal treatment at 130 °C for 24 h. The suspension was thoroughly washed with water to bring the pH near 7. Upon filtration and drying obtained material was pyrolyzed at 600 °C for 2 h in tubular furnace. Zinc ferrite yield from the above-mentioned process was around 1.69 g.

Synthesis of graphene oxide

The chopped banana leaves were oven dried at 100 °C for 24 h and then sieved using 212 micron sieve. 1.69 g of this powdered was dispersed in 70 mL of water and stirred for 30 min. The pH of the solution was raised to 10 using concentrated NaOH and sonication was done as mentioned above, followed by hydrothermal treatment at 130 °C for 24 h. The neutralized suspension was filtered and dried followed by pyrolysis at 600 °C for 2 h in tubular furnace.

Synthesis of ZnFe$_2$O$_4$-rGO nanocomposites

Same synthesis procedure was repeated to prepare $ZnFe_2O_4$ rGO nanocomposites in the weight ratio 3:1, 1:1, 1:3 and 1:6 by mixing 0.56 g, 1.69 g, 5.07 g, 10.12 g of dried banana leaf powder to the zinc ferrite suspension maintained at pH 10. Zinc ferrite, graphene oxide (prepared from the banana leaves), $ZnFe_2O_4$-rGO nanocomposites with ratio 3:1, 1:1, 1:3 and 1:6 was denoted as Z, B, ZB1, ZB2, ZB3 and ZB4, respectively.

Characterization

X-ray powder diffraction patterns for all the powder samples were obtained with a Rigaku- Smart lab diffractometer using Cu Kα1 radiation. The different phases present in the sample

were identified with the relevant JCPDS files. FE-SEM images were captured using FEI-Quanta FEG 200F. The samples were characterized for FT-IR using JASCO 6300 model in the scan region from 400 to 4000 cm^{-1}. The characteristic peaks were compared with the literature and assigned. Nitrogen absorption–desorption isotherm for the BET surface area and BJH pore size distribution was collected using Quantachrome Instruments, Autosorb IQ series. Magnetic properties were tested by vibrating sample magnetometer (Lakeshore). The optical property of samples was studied using the UV–visible (DRS) technique employing Shimadzu UV-2600 UV–vis spectrophotometer. BaSO$_4$ was used as the internal standard. The samples were characterized using Raman spectroscopy (Xplora plus Raman microscope) in the scan region from 100 to 3000 cm^{-1} to identify the nature of carbon present in nanocomposites. The degree of charge carrier recombination for various photocatalysts was investigated utilizing a fluouomax + spectrometer (Horiba Scientific) for photoluminescence (PL) studies. PHI Quantera SXM Scanning X-ray microprobe (ULVAC-PHI, Inc., Japan) was used to measure X-ray photoelectron spectra (XPS) of ZB3.

Photocatalytic activity

Photocatalytic degradation of malachite green and basic yellow dyes was studied using 0.1 g/L of the as-synthesized photocatalytic materials in 100 mL dye solution. 100 W tungsten filament lamp was externally used as the visible light source. For nullifying the adsorption effect, each reaction mixture was magnetically stirred for 30 min in dark to reach the adsorption–desorption equilibrium. The dye solution was periodically withdrawn from the reactor to find the concentration using UV–visible spectrophotometer (Shimadzu UV 2600). λ_{max} at 617 nm and 430 nm were fixed to analyse malachite green and basic yellow dyes, respectively.

Results and discussion

Physio chemical properties

Figure 1 represents the XRD patterns of Z, B, ZB1, ZB2, ZB3 and ZB4. XRD peaks at 30.05°, 35.37°, 42.9°, 53.1°, 56.71°, 62.28° corresponds to (220), (311), (400), (422), (511) and (440) planes of zinc ferrite (JCPDS No. 82–1049 [9]. Peak exhibited at 26.6° corresponds to graphitic framework in sample B. A hump at the lower angle 7 to 10° indicates the presence of small crystallites of graphene oxide [14–16]. Another sharp peak situated at 32.1° corresponds to CaSiO$_3$ [17]. All the ZB materials show the characteristic peaks of zinc ferrite, rGO and CaSiO$_3$. An additional
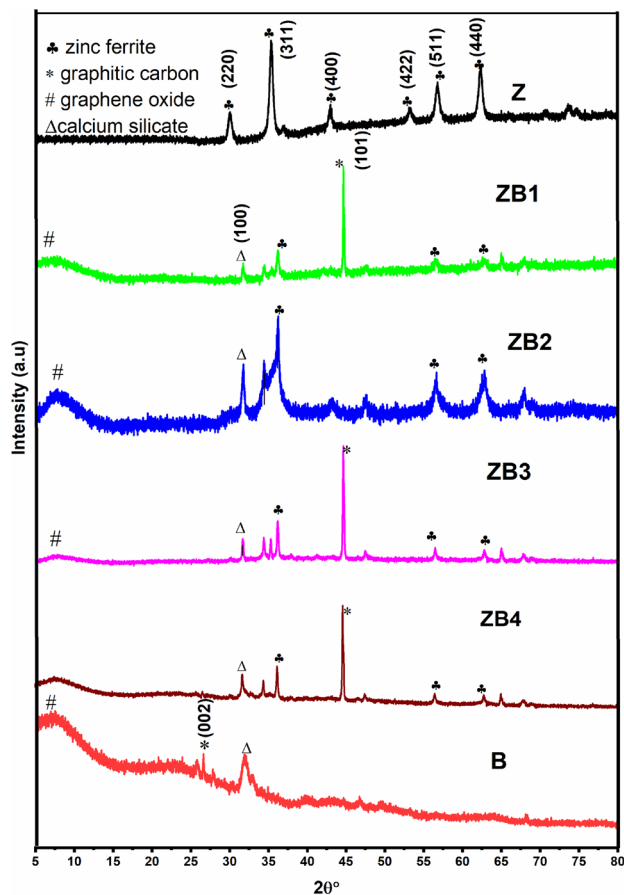

Fig. 1 XRD pattern of different ratio of ZnFe$_2$O$_4$-reduced graphene oxide

peak observed at 44.8° corresponds to (101) plane representing disordered carbon material for ZB materials [18]. The average crystallite size of synthesized materials Z, B, ZB1, ZB2, ZB3 and ZB4 is found to be 19.7 nm, 9 nm, 18.5 nm, 17.6 nm, 5.1 nm and 7.9 nm, respectively. This indicates that there is decrease in zinc ferrite crystallite size on increasing the carbon concentration upto 1:3 ratio. Intercalation of zinc ferrite particles in between the graphitic layers may be attributed for the decreased crystal size. This results in the emergence of rGO which favours the photocatalytic activity.

FE-SEM images represented in Fig. 2 denotes size, shape and morphology of the synthesized materials. Zinc ferrite is spherical and clumsy in nature with average particle size in between 25 and 40 nm. Cross-sectional view of rGO shows the presence of graphene layers with nonuniform pores. These pores are attributed to the removal of volatile matters during pyrolysis. ZB1 shows the hierarchical nano-flower type exfoliated individual rGO due to intercalation of zinc ferrite nanoparticles in between the graphite layers. However, the graphene sheets are highly disordered and contain large amount of corrugations or wrinkles on their surface.

Fig. 2 SEM image of different ratio of ZnFe$_2$O$_4$-reduced graphene oxide photocatalyst **a**. Z **b**. B **c**. ZB1 **d**. ZB2 **e**. ZB3 **f**. ZB4
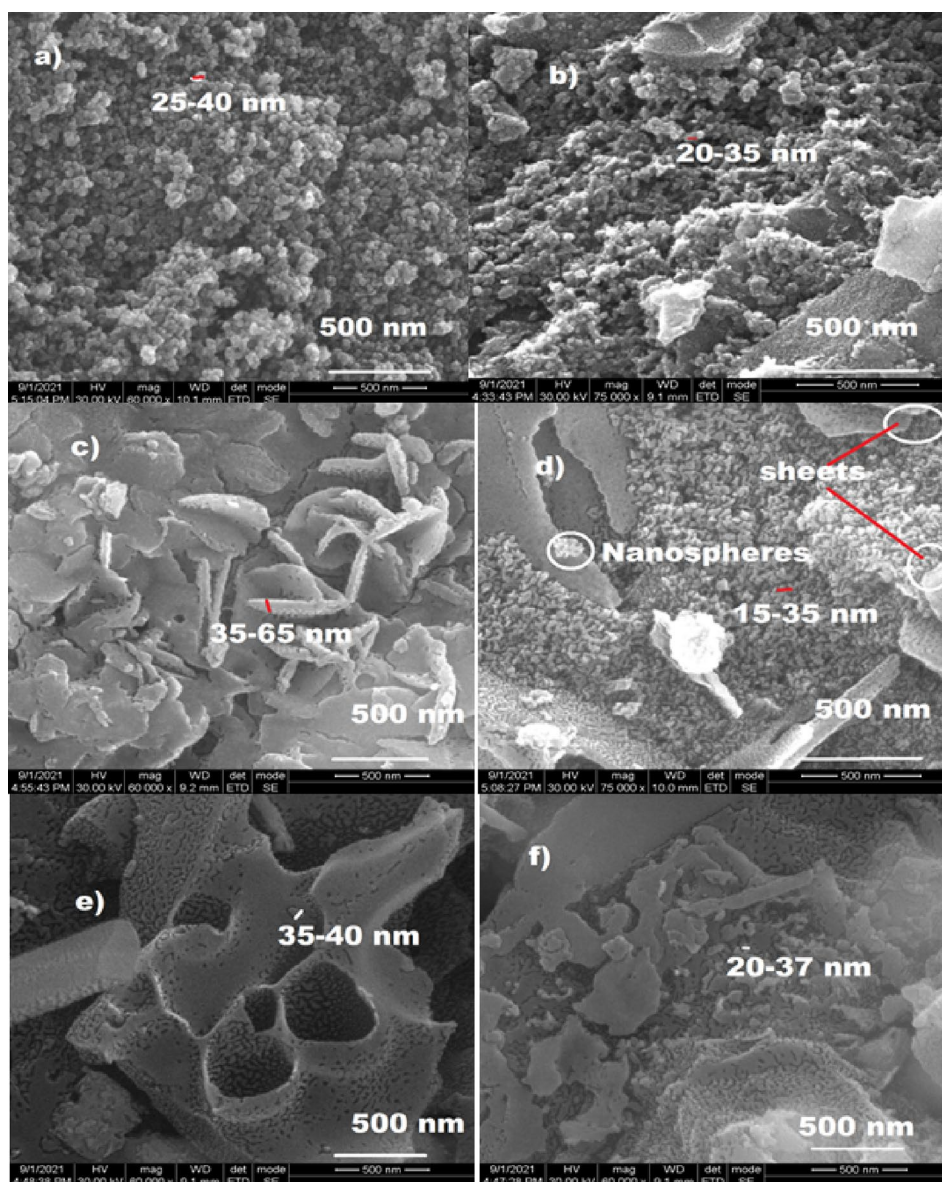
These wrinkles are not point defects but are extended surface defects formed due to the folding or twisting of the few layer graphene sheets. The particle size of B, ZB1, ZB2, ZB3 and ZB4 is calculated using ImageJ and found in the nano-scale range of 20–35 nm, 35–65 nm, 15–35 nm, 35–40 nm and 20–37 nm, respectively. ZB2 and ZB3 confirm the intercalation of zinc ferrite in between the graphene layers. ZB4 having the highest amount of carbon among the composite samples shows the presence of hollow pores. From the EDAX analysis it is found that carbon content for B and ZB3 is 61 and 57 at weight %, whereas oxygen content for ZnFe$_2$O$_4$ is maximum with 23% as shown in Table 1.

Figure 3 represents the FT-IR spectra of the synthesized materials. Peaks at 3440, 540 and 460 cm^{-1} represent the respective OH, Zn–O and Fe–O stretching vibrations present in zinc ferrite [19]. Peaks at 2880 cm^{-1} and 2100 cm^{-1} is

attributed to C–H stretching and allylic –C=C=C– stretching, respectively, in B and ZB samples [20]. 1580 cm^{-1} represents the stretching vibration of conjugated carbon–carbon bonds present in aromatic framework of B and ZB samples. -OH bending at 1440 cm^{-1} and C–O–C stretching at 870 cm^{-1} is present in all the ZB and B samples, clearly indicating the presence of GO moiety [21]. Presence of oxygenated surface is crucial for the photocatalytic reaction in aqueous medium. In all the ZB samples n_1 is observed at 528 cm^{-1} and n_2 at 431 cm^{-1}, which corresponds to intrinsic stretching vibration of Zn–O bonds in tetrahedral sites and Fe–O bonds in octahedral sites [22].
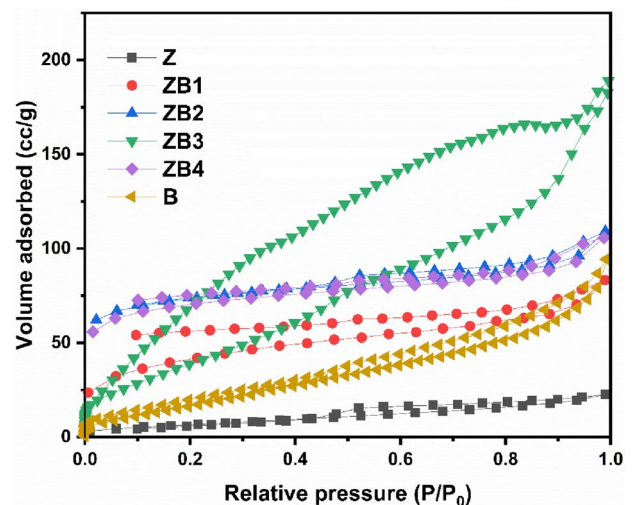
N$_2$ adsorption–desorption curve plotted in Fig. 4 represents Type IV isotherm for zinc ferrite (Z) with hysteresis loop representing narrow split mesopores confirmed by the narrow BJH pore size distribution (Supplementary Fig.S1).

Table 1 EDAX analysis and Nitrogen adsorption/desorption data for the zinc ferrite- reduced graphene oxide (rGO) samples

Sample name	EDAX analysis—Element at wt%				N₂ adsorption/ desorption data	
	C	O	Fe	Zn	Surface area (m^2/g)	Pore volume (cc/g)
Z	5	23	35	17	26	0.035
B	61	18	0	0	75	0.135
ZB1	6	22	32	20	144	0.076
ZB2	10	22	22	18	236	0.208
ZB3	57	16	7	4	342	0.238
ZB4	59	17	3	2	229	0.14
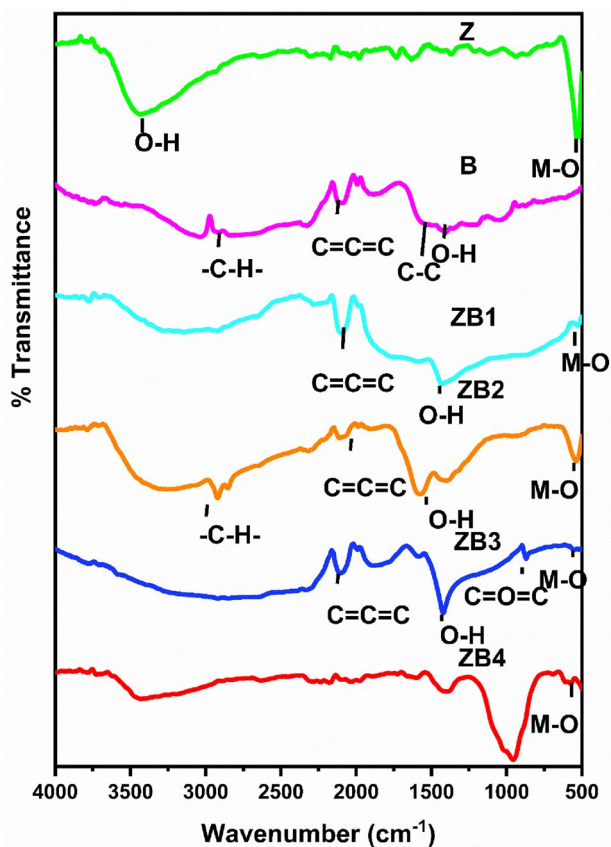
Fig. 3 FTIR curve for different ratio of $ZnFe_2O_4$-reduced graphene oxide

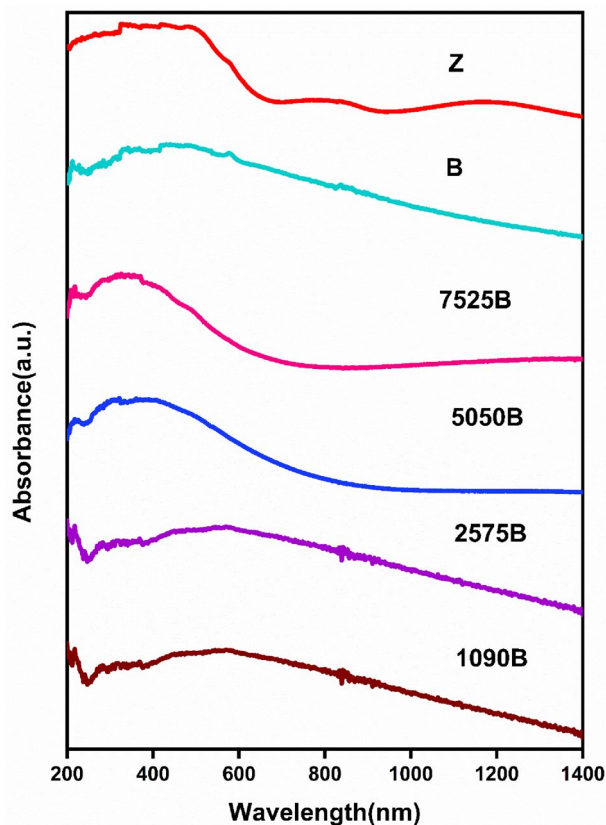**Fig. 4** Adsorption/Desorption curve for different ratio of $ZnFe_2O_4$-reduced graphene oxide

The corresponding BET surface area and the pore volume are 26 m²/g and 0.035 cc/g. Graphene oxide (B) shows Type II isotherm attributed to the multilayer adsorption of N₂ molecules in the macropores [23]. The corresponding BET surface area and the pore volume are 75 m²/g and 0.135 cc/g. ZB1 shows a combination of Type III and Type IV isotherm because of the intercalation of mesoporous zinc ferrite in between the graphite sheet creating macropores which is corroborated from the FE-SEM images also. The corresponding BET surface area and the pore volume of

ZB1 are 144 m²/g and 0.076 cc/g. ZB2 shows the Type IV isotherm with a uniform fissures and irregular thin intercalated sheet like particles in agreement with the FE-SEM images showing H3 hysteresis loop. The corresponding BET surface area and the pore volume are 236 m²/g and 0.208 cc/g. ZB3 and ZB4 show the Type IV isotherms with a H4 hysteresis loops which correspond to narrow mesopores and fissures. The corresponding BET surface area and the pore volume are 342 m²/g and 0.238 cc/g for ZB3, while ZB4 shows the values 229 m²/g and 0.14 cc/g respectively. Pore volume and surface area show an increasing trend from ZB1 < ZB2 < ZB3 as shown in Table 1. In B, the maximum pores are in mesoporous size and there is no uniformity in pore size distribution. The pore size distribution for ZB3 is also good and uniform which helps in more molecules to adsorb on the surface and participate in photocatalytic degradation. In all the samples, even distribution of micropores, mesopores and macropores were illustrated. Uniform pore size distribution along with high pore volume helps in increased adsorption of dye effluents.

Fig.S2 presents the magnetic property of the synthesized materials. All the materials show superparamagnetism because of the small crystallite size as evident from the XRD results. Addition of zinc creates an effective influence in the magnetic properties of the materials [24]. Saturation magnetization improves on increasing the carbon concentration upto ZB3, which may result in the easy magnetic separation of the material from the effluent solution after the photocatalytic treatment [25].

Absorption of visible light is perquisite for the photocatalytic behaviour of the synthesized materials. UV–visible diffuse reflectance and tauc plot represented in Fig. 5 and Fig. S3 indicates the photoresponse of zinc ferrite from visible to NIR range. The absorption edge at 780 nm for zinc ferrite corresponds to bandgap of 1.94 eV. Additional absorption tails at 1180 and > 1400 nm may be due to the defect bands as reported in the literature [26]. Sample B shows the absorption throughout UV–visible and NIR range. The absorption peaks observed at 240 and 320 nm corresponds to $\pi \rightarrow \pi^{*}$ and $n \rightarrow \pi^{*}$ transition for C=C and C=O bond present in graphene oxide [27]. The formation of graphene oxide islands opens up the bandgap in otherwise zero bandgap graphite or graphene. Bandgap of ZB samples lie in between

1.9 and 1.14 eV. Narrowing of the bandgap indicates the interaction between zinc ferrite and graphene oxide. Additionally, the presence of carbon framework functioning as photosensitizer helps in the absorption of more number of photons compared to individual zinc ferrite (Z) [28].

Raman spectra of ZB3 represented in Fig. 6 show the zinc ferrite peaks at 650 cm⁻¹, 450 cm⁻¹ and 355 cm⁻¹ [29]. The presence of D band relates to defective sites, G band for ordered structure and 2D band confirms the graphitic structure. The intense spectrum band around 650 cm⁻¹ in tetrahedral ZnO_4 attributes to A_{1g} symmetric stretching of oxygen. The presence of D and G peak at 1351 cm⁻¹ and 1590 cm⁻¹ in the sample B confirms the formation of graphene oxide (GO). In contrast, in ZB3 the D and G bands are shifted to 1327 cm⁻¹ and 1563 cm⁻¹, respectively. Few layers rGO formation is confirmed because of Intense G band and less intense 2D band. The 2D region appears due to exfoliation and reduction. Broadening of the G band in synthesised sample indicates the formation of thermally exfoliated graphene (TEG) [30]. The I_D/I_G ratio of B and ZB3 increased from 0.86 to 0.92, indicating the formation of sp² domains working as defective rGO. This can be corroborated with increase magnetic properties which was proved best at 700 °C [31].

Fig. 5 Absorbance curve for different ratio of $ZnFe_2O_4$-reduced graphene oxide photocatalyst
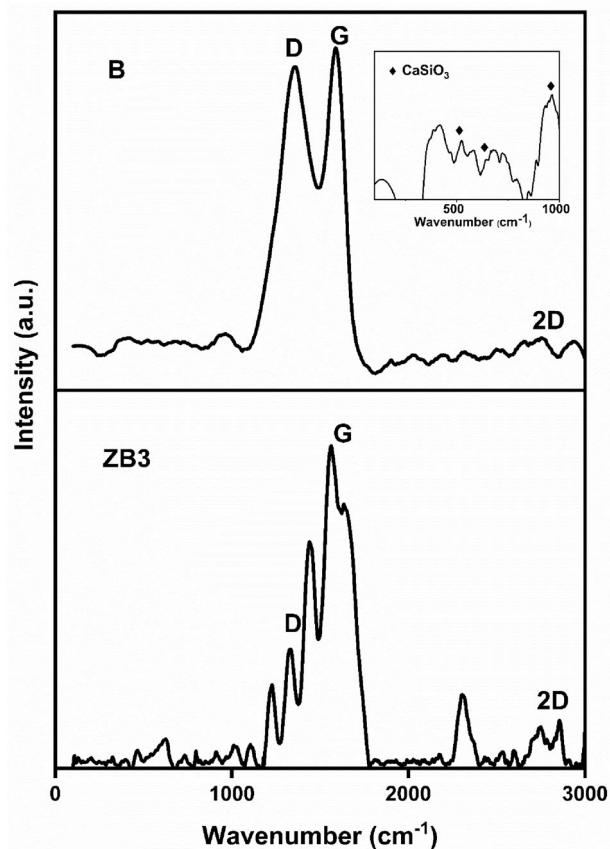
Fig. 6 Raman Spectra of B and ZB3

The ratio of I_{2D}/I_G helps to reveal the number of graphene layer present in the material. Ratio of I_{2D}/I_G around 3–2, 2–1 and < 1 validates the formation of monolayer, bilayer and multilayer graphene, respectively. In B and ZB3 samples the obtained I_{2D}/I_G ratio is 1.73 and 1.83 which corroborates the presence of bilayer graphene [32]. The peaks obtained at 521 cm^{-1}, 645 cm^{-1} and 972 cm^{-1} indicate the presence of $CaSiO_3$ [33]. GO is highly functional derivative with hydroxyl (C–OH), carbonyl(C=O) and carboxyl (-COOH) groups. rGO boosts the efficient photo-induced charges separation that results in enhanced photocatalytic properties of the material.

The XPS spectra of C1s band of ZB3 are shown in Fig. 7a. The peaks obtained at 284.8, 285.5 and 288.5 eV corroborates with respective binding energies of sp^2 C–C, C–O and O–C=O transitions, respectively [34]. Peaks at 286.1 and 291.4 eV are due to C–O–C and $\pi \rightarrow \pi^*$ transition in GO, as observed in UV–visible spectra [35], 27. The two major peaks observed at 1045.9 and 1022.7 eV in Fig. 7b correspond to the Zn 2p$_{1/2}$ and Zn 2p$_{3/2}$ peaks, in agreement with the spinel structure $ZnFe_2O_4$ [36, 37]. Fe 2p spectrum shown in Fig. 7c gives couple of peaks at 711.3 and 724.7 eV corresponding to Fe 2p$_{1/2}$ and Fe 2p$_{3/2}$ [38]. Fe^{3+} present in $ZnFe_2O_4$ is confirmed by the presence of

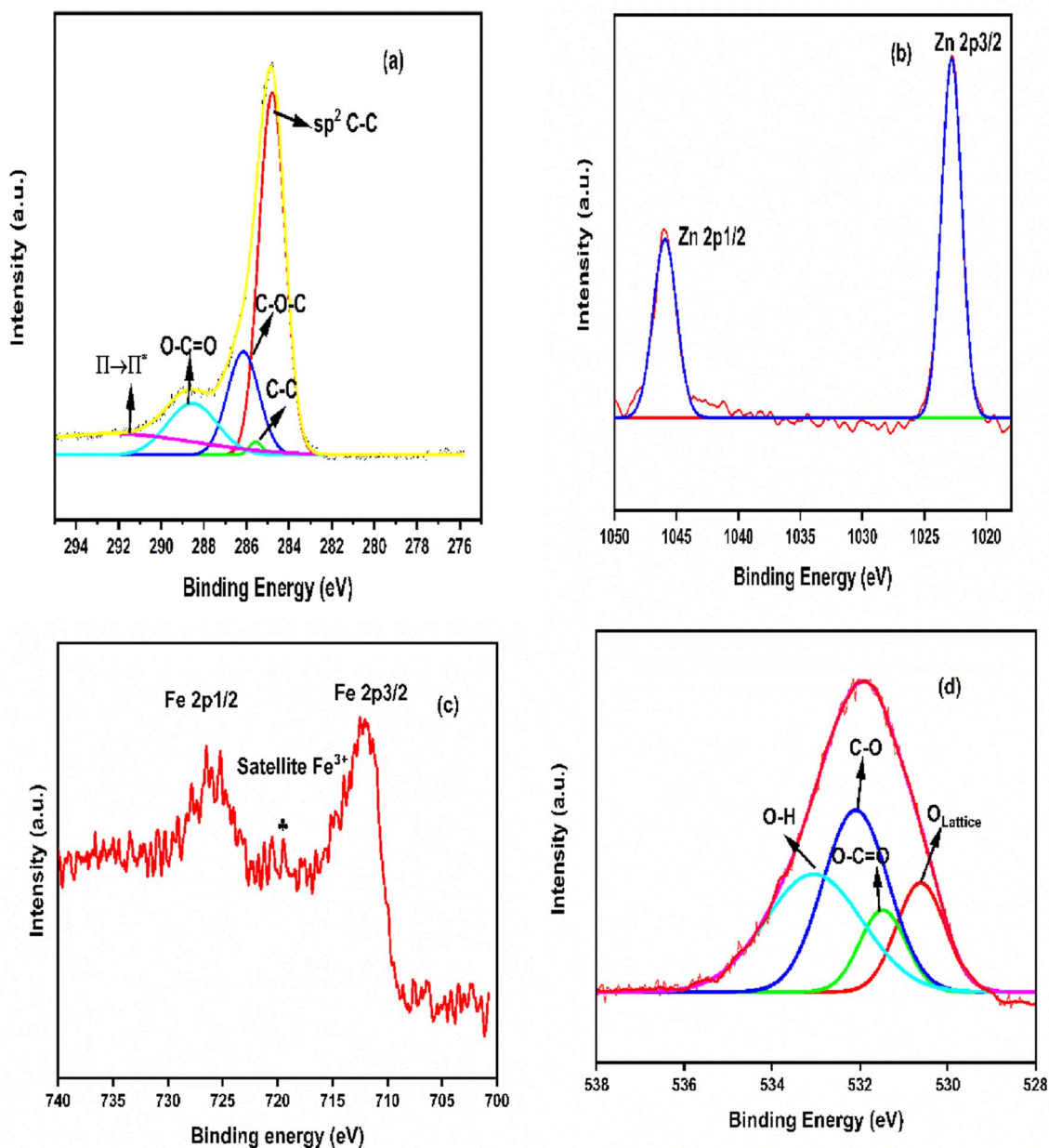**Fig. 7** XPS spectra of ZB3 **a** C 1 s **b** Zn 2p **c** Fe 2p **d** O 1 s

satellite peak at $719.4 - 720.4$ eV [37]. This corroborates the formation of Fe–O bonds in octahedral sites as mentioned in FT-IR. Figure 7d represents the O 1 s peaks with binding energies at 530.6 and 531.4 eV corresponds to lattice oxygen bonding and O–C=O. Other peaks with binding energies at 532.09 and 533.05 eV correspond to C–O and O–H [5, 39]. The surface-absorbed oxygen species gets ionized by the adsorbed oxygen molecules resulting in the formation of reactive oxygen species (O^{2-}, O^- and O_2^-) [37].

Fig. S4 displays the PL emission spectra of as-synthesised materials excited at 385 nm. PL intensity of ZB3 is observed to be less intense compared to Z. The presence of rGO in ZB3 helps in more efficient electron–hole pair separation which favours the photocatalytic activity. This finding supports the effective electron transfer which in turn supports the higher level of hydroxyl radicals generation which is vital for photocatalytic degradation [5].

Photocatalytic activity

Visible light photocatalytic activity of malachite green is examined using the synthesized materials (Fig. 8). The decomposition of dye molecules is shown in the absorption peak shift (Fig. 8a). The control experiment exhibits negligible degradation of MG in absence of photocatalyst powder, indicating no photolysis of the dye. The effect of photocatalytic materials variation shows the degradation efficiency following ZB3 > ZB2 > ZB1 > ZB4 > B trend. ZB3 achieves the complete degradation of MG within 60 min, whereas Z and B could achieve only 25 and 20% degradation, respectively. Higher activity of ZB3 may be attributed to its small crystallite size, high surface area, extended visible-NIR light absorption and formation of $ZnFe_2O_4$–rGO heterojunction owing to the intercalation of $ZnFe_2O_4$ in between the graphite layers. Based on the flat band potential of $ZnFe_2O_4$ reported in the literature -0.09 eV (RHE) and the bandgap of 1.94 eV obtained from Fig. S3 [40], the conduction band and valence band are suggested to be positioned at -0.09 and $+1.46$ eV, respectively. The visible light excited electrons in $ZnFe_2O_4$ are transported along the layer of graphene oxide thereby separating the electron–hole pairs resulting in improved activity [41]. The corresponding ln (C_0/C) plot follows characteristics of linear pseudo-first-order reaction with R^2 value as 0.97. Figure 7b represents the effect of different synthesized materials of ZB towards MG concentration on the photocatalytic degradation. Photocatalytic degradation increases with the increase in concentration of MG upto 50 ppm there after degradation decrease on increasing the concentration further (Fig. 8c, e). The number of active sites present on the photocatalyst surface plays an important role in the degradation process. On increasing the dye molecule concentration, a greater number of active sites are occupied reaching a threshold of 50 ppm. A plot of ln (C_0/C) vs time for different concentration gives a linear line, indicating pseudo-first-order reaction kinetics (Fig. 8f). pH of the reaction mixture is an important factor influencing the heterogeneous photocatalysis. As the MG fades above pH 10 the pH values selected include 3, 7 and 9 to study the effect of pH variation. 30, 83 and 100% degradation of MG is achieved at pH 3, 9 and 7, respectively (Fig. 8d). Point of zero charge (pH_{zpc}) of the zinc ferrite and activated carbon reported in the literature is 5.6 and 6.2, respectively [42]. Below the pH_{zpc} photocatalytic surface will be electrostatically positively charged, whereas at higher pH the surface will be negatively charged. Highest activity achieved at pH 7 is because of favourable interaction between the negatively charged ZB3 and positively charged MG, whereas low degradation at pH 3 is attributed to the electrostatic repulsion between the positively charged ZB3 surface and the cationic MG. Dissolved oxygen present in the solution captures the photogenerated electrons to form $\cdot O_2^-$ free radicals which helps in the degradation of the MG dye. pH value is around 6.5 to 6.7 before degradation and it reaches around 7.1 to 7.3 after degradation of MG dye.

Fig. S5 a shows the degradation peak curve of 50 ppm BY dye with ZB3. Fig. S5 b elaborates the degradation of BY with respect to different synthesized materials and it is found that there is only a negligible degradation of BY without catalyst. Basic yellow 28 dye (BY) shows the similar degradation trend as MG for the material variation. The presence of rGO resulted in significant removal of MG and BY which is in agreement with the reported literatures [43]. Fig. S5 c shows the pollutant concentration variation with highest degradation of about 98% for 50 ppm. The increase in pollutant concentration will result in occupancy of more adsorption of amount of dye molecules on the catalyst surface resulting in decrease in penetration of light required for the process [44]. Photocatalytic activity of BY differs from MG in alkaline pH (Fig. S5 d). This may be due to higher electrostatic attractions between the negatively charged ZB3 and positively charged BY functional group [45, 46]. Initial degradation of more than 40% is achieved at the time interval of 20 min for ZB3, which may be attributed due to the presence of more number of active sites. Because of the cationic nature of BY28, it is expected that the reaction rate would be higher at pH values above pHzpc of the synthesized material. Here the availability of negative charges on ZB3 increases at alkaline condition (pH 10) thereby resulting in complete degradation of BY within 60 min of time. pH value is around 6.6 to 6.9 before degradation and
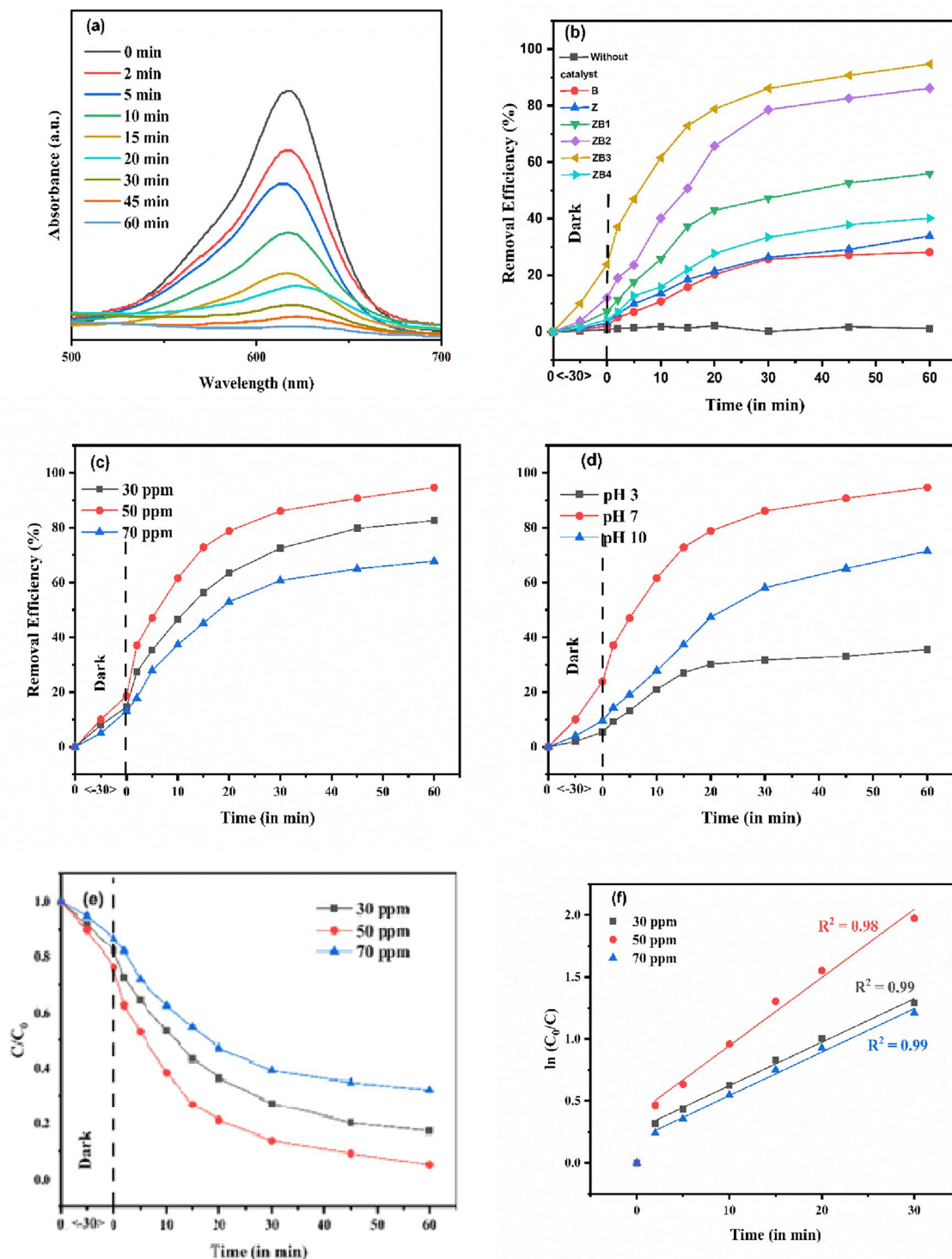
Fig. 8 Degradation of malachite green dye **a** Intensity change with irradiation time **b** Effect of different ratio of photocatalyst **c** Effect of pollutant concentration **d** Effect of pH variation **e** Photocatalytic degradation at various concentration **f** Plot of ln (Co/C) versus time

it reaches 7.5 after degradation of BY dye. Similar studies with rGO/ZnFe$_2$O$_4$ produced by one-step solvothermal process shows that 100% methylene blue dye degradation

at 120 min [47]. rGO/ZnFe$_2$O$_4$ produced by hydrothermal method shows ciprofloxin degradation of about 73.4% after 60 min [48].

Conclusions

Nanoflower type Zinc ferrite-rGO in 3:1, 1:1, 1:3 and 1:6 ratio was successfully synthesized by hydrothermal cum pyrolysis method using banana leaves as the carbon source. Powder diffraction results indicate the presence of zinc ferrite, reduced graphene oxide and $CaSiO_3$. FE-SEM micrographs represent the intercalation of zinc ferrite particles in between the graphite layers to form graphene oxide islands. Surface area and pore volume increased to 342 m^2/g and 0.238 cc/g for ZB3. All the materials exhibit superparamagnetism with increase in saturation magnetization on increasing the carbon ratio till ZB3. DRS shows the absorption peaks of graphene oxide with narrowing of bandgap from 1.9 to 1.14 eV due to interaction between reduced graphene oxide and zinc ferrite, which resulted in increase in the electron–hole pair formation. Raman spectrum confirms the presence of the bilayer rGO and $CaSiO_3$ in the synthesized samples. ZB3 is able to degrade the cationic dyes malachite green (MG) and basic yellow 28 (BY) within 60 min of visible light irradiation. The optimum conditions were obtained at pH 7 and pH 10 for MG and BY dyes, respectively. Higher activity of ZB3 is ascribed to its small crystallite size, high surface area, extended visible-NIR light absorption and formation of $ZnFe_2O_4$-rGO heterojunction owing to the intercalation of $ZnFe_2O_4$ in between the graphite layers. The successful exploration of the use of banana leaves in the synthesis of reduced graphene oxide (rGO) provides a pathway for more environmentally friendly synthesis using biomass.

Data availability statement The datasets generated during and/or analysed during the current study are available from the corresponding author on reasonable request.

Declarations

Conflict of interest The authors declare that they have not known competing financial interests or personal relationships that could have appeared to influence the work reported in this paper.

References

1. Sarkar S, Banerjee A, Halder U et al (2017) Degradation of synthetic azo dyes of textile industry: a sustainable approach using microbial enzymes. Water Conserv Sci Eng 2:121–131. https://doi.org/10.1007/s41101-017-0031-5

2. Gupta VK, Suhas, (2009) Application of low-cost adsorbents for dye removal—a review. J Environ Manage 90:2313–2342. https://doi.org/10.1016/j.jenvman.2008.11.017

3. Ali H (2010) Biodegradation of synthetic dyes: a review. Water Air Soil Pollut 213:251–273. https://doi.org/10.1007/s11270-010-0382-4

4. Deng Y, Zhao R (2015) Advanced oxidation processes (AOPs) in wastewater treatment. Curr Pollut Reports 1:167–176. https://doi.org/10.1007/s40726-015-0015-z

5. Magadevan D, Lakshmi T, Mundari NDA et al (2022) Construction of Ag3PO4–TiO2 nano-heterostructure with excellent visible-light-driven photocatalytic activity for environmental applications. Nanotechnol Environ Eng. https://doi.org/10.1007/s41204-022-00261-1

6. Ahmed S, Rasul MG, Martens WN et al (2011) Advances in heterogeneous photocatalytic degradation of phenols and dyes in wastewater: a review. Water Air Soil Pollut 215:3–29. https://doi.org/10.1007/s11270-010-0456-3

7. Yang Y, Liu X, Yang Y et al (2013) Synthesis of nonstoichiometric zinc ferrite nanoparticles with extraordinary room temperature magnetism and their diverse applications. J Mater Chem C 1:2875–2885. https://doi.org/10.1039/c3tc00790a

8. Ajormal F, Moradnia F, TaghaviFardood S, Ramazani A (2020) Zinc ferrite nanoparticles in photo-degradation of dye: mini-review. J Chem Rev 2:90–102. https://doi.org/10.33945/sami/jcr.2020.2.2

9. Lu D, Zhang Y, Lin S et al (2013) Synthesis of magnetic ZnFe2O4/graphene composite and its application in photocatalytic degradation of dyes. J Alloys Compd 579:366–372. https://doi.org/10.1016/j.jallcom.2013.06.098

10. Yang C, de Falco G, Florent M et al (2021) The effect of ZnFe2O4/activated carbon adsorbent photocatalytic activity on gas-phase desulfurization. Chem Eng J 423:130255. https://doi.org/10.1016/j.cej.2021.130255

11. Ye J, Liu SQ, Liu WX et al (2019) Photocatalytic simultaneous removal of nitrite and ammonia via a zinc ferrite/activated carbon hybrid catalyst under UV-visible irradiation. ACS Omega 4:6411–6420. https://doi.org/10.1021/acsomega.8b00677

12. Tajik S, Askari MB, Ahmadi SA et al (2022) Electrochemical sensor based on ZnFe2O4/RGO nanocomposite for ultrasensitive detection of hydrazine in real samples. Nanomaterials 12:1–10. https://doi.org/10.3390/nano12030491

13. Simfukwe J, Mapasha RE, Braun A, Diale M (2017) Biopatterning of keratinocytes in aqueous two-phase systems as a potential tool for skin tissue engineering. MRS Adv 357:1–8. https://doi.org/10.1557/adv.201

14. Blanton TN, Majumdar D (2013) Characterization of X-ray irradiated graphene oxide coatings using X-ray diffraction, X-ray photoelectron spectroscopy, and atomic force microscopy. Powder Diffr 28:68–71. https://doi.org/10.1017/S0885715613000109

15. Sreeja VG, Vinitha G, Reshmi R et al (2017) Effect of reduction time on third order optical nonlinearity of reduced graphene oxide. Opt Mater (Amst) 66:460–468. https://doi.org/10.1016/j.optmat.2017.01.042

16. Joshi NC, Congthak R, Gururani P (2020) Synthesis, adsorptive performances and photo-catalytic activity of graphene oxide/TiO2 (GO/TiO2) nanocomposite-based adsorbent. Nanotechnol Environ Eng 5:1–13. https://doi.org/10.1007/s41204-020-00085-x

17. Wang H, Zhang Q, Yang H, Sun H (2008) Synthesis and microwave dielectric properties of CaSiO3 nanopowder by the sol-gel process. Ceram Int 34:1405–1408. https://doi.org/10.1016/j.ceramint.2007.05.001

18. Hidayah NMS, Liu WW, Lai CW et al (2017) Comparison on graphite, graphene oxide and reduced graphene oxide: synthesis

and characterization. AIP Conf Proc. https://doi.org/10.1063/1.5005764

19. Nadeem N, Zahid M, Tabasum A et al (2020) Degradation of reactive dye using heterogeneous photo-Fenton catalysts: ZnFe2O4 and GO-ZnFe2O4 composite. Mater Res Express 7:15519. https://doi.org/10.1088/2053-1591/ab66ee

20. Islam MS, Ang BC, Gharehkhani S, Afifi ABM (2016) Adsorption capability of activated carbon synthesized from coconut shell. Carbon Lett 20:1–9. https://doi.org/10.5714/CL.2016.20.001

21. He D, Peng Z, Gong W et al (2015) Mechanism of a green graphene oxide reduction with reusable potassium carbonate. RSC Adv 5:11966–11972. https://doi.org/10.1039/c4ra14511a

22. Lima ES, Costa LS, Sampaio GRLM et al (2019) Zinc ferrite nanoparticles via coprecipitation modified method: Glycerol as structure directing and stabilizing agent. J Braz Chem Soc 30:882–891. https://doi.org/10.21577/0103-5053.20180225

23. Alothman ZA (2012) A review: fundamental aspects of silicate mesoporous materials. Materials (Basel) 5:2874–2902. https://doi.org/10.3390/ma5122874

24. Kurmude DV, Kale CM, Aghav PS et al (2014) Superparamagnetic behavior of zinc-substituted nickel ferrite nanoparticles and its effect on mossbauer and magnetic parameters. J Supercond Nov Magn 27:1889–1897. https://doi.org/10.1007/s10948-014-2535-y

25. Manikandan A, Judith Vijaya J, Sundararajan M et al (2013) Optical and magnetic properties of Mg-doped ZnFe2O4 nanoparticles prepared by rapid microwave combustion method. Superlattices Microstruct 64:118–131. https://doi.org/10.1016/j.spmi.2013.09.021

26. Chen H, Liu W, Qin Z (2017) ZnO/ZnFe2O4 nanocomposite as a broad-spectrum photo-Fenton-like photocatalyst with near-infrared activity. Catal Sci Technol 7:2236–2244. https://doi.org/10.1039/c7cy00308k

27. Johra FT, Lee JW, Jung WG (2014) Facile and safe graphene preparation on solution based platform. J Ind Eng Chem 20:2883–2887. https://doi.org/10.1016/j.jiec.2013.11.022

28. Hou J, Jiang K, Shen M et al (2017) Micro and nano hierachical structures of BiOI/activated carbon for efficient visible-light-photocatalytic reactions. Sci Rep 7:2–11. https://doi.org/10.1038/s41598-017-12266-x

29. Bini M, Tondo C, Capsoni D et al (2018) Superparamagnetic ZnFe2O4 nanoparticles: the effect of Ca and Gd doping. Mater Chem Phys 204:72–82. https://doi.org/10.1016/j.matchemphys.2017.10.033

30. Kaniyoor A, Ramaprabhu S (2012) A Raman spectroscopic investigation of graphite oxide derived graphene. AIP Adv. https://doi.org/10.1063/1.4756995

31. Kurniasari MA, Nugraheni AY et al (2017) Defect and Magnetic Properties of Reduced Graphene Oxide Prepared from Old Coconut Shell. IOP Conf Ser Mater Sci Eng 196:012021. https://doi.org/10.1088/1757-899X/196/1/012021

32. Nguyen VT, Le HD, Nguyen VC et al (2013) Synthesis of multilayer graphene films on copper tape by atmospheric pressure chemical vapor deposition method. Adv Nat Sci Nanosci Nanotechnol. https://doi.org/10.1088/2043-6262/4/3/035012

33. Zedgenizov DA, Ragozin AL, Kalinina VV, Kagi H (2016) The mineralogy of Ca-rich inclusions in sublithospheric diamonds. Geochemistry Int 54:890–900. https://doi.org/10.1134/S0016702916100116

34. Han J, Jun BM, Heo J et al (2019) Highly efficient organic dye removal from waters by magnetically recoverable La2O2CO3/ZnFe2O4-reduced graphene oxide nanohybrid. Ceram Int 45:19247–19256. https://doi.org/10.1016/j.ceramint.2019.06.173

35. Vázquez-Samperio J, Sánchez-Padilla NM, Acevedo-Peña P et al (2018) Ni prussian blue analogue/mesoporous carbon composite as electrode material for aqueous K-ion energy storage: effect of carbon-framework interaction on its electrochemical behavior. ChemistrySelect 3:11441–11450. https://doi.org/10.1002/slct.201801333

36. Muthuvel A, Jothibas M, Manoharan C (2020) Effect of chemically synthesis compared to biosynthesized ZnO-NPs using Solanum nigrum leaf extract and their photocatalytic, antibacterial and in-vitro antioxidant activity. J Environ Chem Eng 8:103705. https://doi.org/10.1016/j.jece.2020.103705

37. Ma X, Zhou X, Gong Y et al (2017) MOF-derived hierarchical ZnO/ZnFe2O4 hollow cubes for enhanced acetone gas-sensing performance. RSC Adv 7:34609–34617. https://doi.org/10.1039/c7ra04437b

38. Yamashita T, Hayes P (2008) Analysis of XPS spectra of Fe 2+ and Fe 3+ ions in oxide materials. Appl Surf Sci 254:2441–2449. https://doi.org/10.1016/j.apsusc.2007.09.063

39. Liu C, Jia M, Qu J et al (2020) Intermolecular hydrogen bonding between poly[(R)-3-hydroxybutyrate] (PHB) and pseudoboehmite and its effect on crystallization of PHB. ACS Appl Polymer Mater 2(11):4762–4769

40. Behera A, Kandi D, Majhi SM et al (2018) Facile synthesis of ZnFe2O4 photocatalysts for decolourization of organic dyes under solar irradiation. Beilstein J Nanotechnol 9:436–446. https://doi.org/10.3762/bjnano.9.42

41. Li F, Jiang X, Zhao J, Zhang S (2015) Graphene oxide: a promising nanomaterial for energy and environmental applications. Nano Energy 16:488–515. https://doi.org/10.1016/j.nanoen.2015.07.014

42. Ibrahim I, Ali IO, Salama TM et al (2016) Synthesis of magnetically recyclable spinel ferrite (MFe2O4, M=Zn Co, Mn) nanocrystals engineered by sol gel-hydrothermal technology: high catalytic performances for nitroarenes reduction. Appl Catal B Environ 181:389–402. https://doi.org/10.1016/j.apcatb.2015.08.005

43. Baruah S, Kumar S, Nayak B, Puzari A (2021) Optoelectronically suitable graphene oxide-decorated titanium oxide/polyaniline hybrid nanocomposites and their enhanced photocatalytic activity with methylene blue and rhodamine B dye. Polym Bull 78:1703–1720. https://doi.org/10.1007/s00289-020-03182-8

44. Daneshvar N, Salari D, Khataee AR (2003) Photocatalytic degradation of azo dye acid red 14 in water: Investigation of the effect of operational parameters. J Photochem Photobiol A Chem 157:111–116. https://doi.org/10.1016/S1010-6030(03)00015-7

45. Lee CK, Liu SS, Juang LC et al (2007) Application of MCM-41 for dyes removal from wastewater. J Hazard Mater 147:997–1005. https://doi.org/10.1016/j.jhazmat.2007.01.130

46. Juang LC, Wang CC, Lee CK (2006) Adsorption of basic dyes onto MCM-41. Chemosphere 64:1920–1928. https://doi.org/10.1016/j.chemosphere.2006.01.024

47. Jenita Rani G, Rajan J (2017) Reduced graphene oxide/ZnFe2O4 nanocomposite as an efficient catalyst for the photocatalytic degradation of methylene blue dye. Res Chem Intermed 43:2669–2690. https://doi.org/10.1007/s11164-016-2788-0

48. Behera A, Kandi D, Mansingh S et al (2019) Facile synthesis of ZnFe2O4@RGO nanocomposites towards photocatalytic ciprofloxacin degradation and H2 energy production. J Colloid Interface Sci 556:667–679. https://doi.org/10.1016/j.jcis.2019.08.109